

Reproducing the Solar System Acceleration Detection from Gaia Early Data Release 3 (A & A)

A Report Presented
By
Matteo Mancini

Department
Department of Physics

Degree
MPhil Data Intensive Science

Project Supervisor
Dr. Christopher J. Moore

Word Count:
7097

GitHub:
https://github.com/MatteoMancini01/Gaia_EDR3

Easter Term 2025

Abstract

We present an independent reproduction of the solar system acceleration measurement reported in Gaia EDR3, using extragalactic sources as a non-rotating reference frame. Adopting a Bayesian inference approach based on vector spherical harmonics, we obtain results consistent with Klioner et al. (2021) in both magnitude and direction. Additionally, we explore the robustness of the inferred acceleration under varying outlier rejection thresholds and analyse the power spectral distribution of the VSH coefficients. Our findings reinforce the reliability of Gaia-based acceleration detection and validate alternative statistical methodologies.

Acknowledgment

I would like to express my sincere gratitude to my project supervisor, Dr. Christopher J. Moore, for his guidance and support in making this project possible.

Contents

1	Introduction	1
2	Background	1
2.1	Overview of Gaia mission and Early Data Release 3 (EDR3)	1
2.2	Proper Motion & Reference Frame	1
2.3	Theoretical Basis for Detecting Solar Acceleration	2
2.3.1	Expected Magnitude and Direction	3
2.3.2	Perturbation from Galactic and Extragalactic Structure	3
2.3.3	Why Use Quasars?	4
2.4	Vector Spherical Harmonics (VSH) Framework	4
2.4.1	Definition	4
3	Data & Preprocessing	6
3.1	QSO Sample Selection	6
3.2	Filtering and Quality Cuts	6
3.3	Galactic Object	11
4	Methods	11
4.1	Frequentist Approach	12
4.2	Bayesian Approach	12
4.2.1	Choice of Prior	13
4.2.2	Likelihood Function	13
5	Analysis & Results	13
5.1	Summary of Results	16
5.2	Further Tests	18
5.2.1	Power Spectral Distribution (PSD) of VSH Coefficients	18
5.2.2	Impact of Clipping Thresholds on Acceleration Estimates	19
6	Conclusion	22
A	Use of Auto-Generation Tools	25
A.1	Copilot	25
A.2	Chat-GPT4	25
B	Trace Plots	25
C	Different Prior	25

List of Figures

1	Sky distribution of Gaia-CRF3 QSO-like sources in Galactic coordinates, shown as source density per square degree using HEALPix binning ($N_{\text{side}} = 64$). The density is computed from the five-parameter subset of the Gaia EDR3 AGN catalogue. Regions near the Galactic plane are masked or show low source density due to strong extinction and stellar contamination. The map uses a Mollweide projection with a linear colour scale ranging from 0 to 80 ANGs per deg ²	7
2	Sky distribution of the statistical weights used in the proper motion analysis, shown in Galactic coordinates with HEALPix binning ($N_{\text{side}} = 64$). Each pixel shows the sum of inverse squared uncertainties in proper motion, $\sigma_{\mu_{\alpha^*}}^{-2} + \sigma_{\mu_{\delta}}^{-2}$, for all sources in that pixel. Brighter regions correspond to areas with the higher astrometric precision and/or more sources. The white band near the Galactic plane reflects masked or excluded regions due to high stellar contamination or astrometric uncertainty.	8
3	Distributions of key astrometric parameters for the Gaia-CRF3 sources with five-parameter solutions: G-band magnitude (top), effective wavenumber ν_{eff} (middle), and RUWE (bottom). All distributions are shown on logarithmic scale highlight tails and outliers. These properties inform both astrometric quality and filtering decisions in the analysis.	9
4	Distributions of normalised astrometric quantities for Gaia-CRF3 sources with five-parameter solutions: parallax (top), proper motion in RA μ_{α^*} (middle), and proper motion in declination μ_{δ} (bottom), each divided by their formal uncertainty. These distributions are expected to approximate standard normal distributions if the uncertainties are well estimated and the sources have negligible true values, as expected for distant quasars.	10
5	Equatorial (top figure) and galactic (bottom figure) components of the solar system acceleration as a function of l_{max} . The error bars are within $\pm 1\sigma$ uncertainty. Compare with Figure 7, Section 7 of Klioner et al., 2021. It is important to notice that outlier detection was performed Figure 7 of Klioner et al. (2021), and they rejected ~ 3800 per l_{max} , however we did not remove any outliers to produce this plot.	14
6	Equatorial components of the acceleration vector (g_x, g_y, g_z) estimated from QSO-like sources binned by Gaia G -band magnitude: $G \leq 18$ (29 200 sources), $18 < G \leq 19$ (146 614 sources), $19 < G \leq 20$ (490 161 sources), and $G > 20$ (549 967 sources). Error bars represent 1σ uncertainties from posterior sampling in each bin. The shaded horizontal bands indicate the values and associated uncertainties ($\pm 1\sigma$, the height corresponds to twice the uncertainty) for each component derived from the full dataset, independent of magnitude. This comparison illustrates the stability of the acceleration signal across different magnitude ranges.	15
7	Equatorial components of the associated acceleration vector along with their associated uncertainties, shown across four intervals of the effective wavenumber ν_{eff} , distribution in the selected dataset, ensuring each bin contains $\sim 304\,000$ sources. The shaded horizontal bands represents the values and uncertainties (with width equal to twice the uncertainty) computed from the full sample, serving as a reference for comparison.	16
8	2D joint distribution of the RA and Dec samples. The red cross indicates the location of the Galactic centre, located at $\alpha \approx 266.42^\circ$, $\delta \approx -29.01$ (M. J. Reid and Brunthaler, 2004).	18
9	Violin plots showing the power spectral distribution (PSD) of the VSH coefficient samples as a function of harmonic degree l_{max} . The top panel corresponds to the toroidal components, and the bottom panel to the spheroidal components. Each distribution reflects the spread and median of the posterior power for each l mode.	19
10	Left: Posterior distributions of the VSH coefficients (parameter θ) obtained from all chains. Right: Corresponding trace plots for each parameter across iterations, illustrating chain mixing and convergence.	25

List of Tables

1	Final estimate of the Solar System acceleration vector. All the uncertainties are within $\pm 1\sigma$, these are obtained from HMC sampling.	17
2	Estimate of the Solar System acceleration vector using HMC sampling on data filtered with clipping threshold $\kappa = 2.0$, 79 550 sources were detected as outliers. All uncertainties are at the 1σ level.	20
3	Estimate of the Solar System acceleration vector using HMC sampling on data filtered with clipping threshold $\kappa = 4.0$, 41 sources were detected as outliers. All uncertainties are reported at the 1σ level.	21
4	Estimate of the Solar System acceleration vector using HMC sampling on the full (unfiltered) five-parameter Gaia EDR3 dataset. All uncertainties are reported at the 1σ level. .	21
5	Estimate of the Solar System acceleration vector using HMC sampling with uniform prior.	26

1 Introduction

The primary objective of this project is to independently reproduce the results presented in the Gaia Early Data Release 3 (EDR3) study on the detection of the Solar System’s acceleration through astrometric measurements of extragalactic sources, as detailed in Klioner et al. (2021). By following the methodological framework outlined in that study, we aim to verify the robustness and reproducibility of their findings, using vector spherical harmonics (VSH) to model the proper motion field of distant quasars.

The EDR3 analysis provides a compelling approach to inferring the Solar System’s acceleration by treating extragalactic quasars as a non-rotating reference frame. This assumption allows one to extract systematic dipole patterns in the proper motion field, which arise due to the solar barycentre’s acceleration. Section 2 summarises the relevant theoretical background, including the VSH formalism and the physical motivations for using quasars in this context.

In Section 3, we describe the criteria used to select the sample of extragalactic sources and outline the preprocessing steps performed on the Gaia EDR3 data. Our methodology is detailed in Section 4, where we compare our Bayesian inference pipeline to the original frequentist analysis used in Klioner et al. (2021). Finally, Section 5 presents the core results of our analysis, including various robustness tests and consistency checks across data subsets.

Additional technical details, including validation diagnostics, propagation of uncertainty, and supplementary discussions, are provided in the appendices.

2 Background

This section aims to introduce the theoretical aspects of solar acceleration, and vector spherical harmonics geometry. The idea that the solar system’s acceleration could induce apparent proper motions in distant objects dates back to the 19th century. John Pond (1833) first speculated on the phenomenon, though observational capabilities at the time were inadequate. Interest revived in the VLBI era (Fanselow and Sovers (1985)) and became a stated science objective of the Gaia mission (Perryman and van Leeuwen (1995)). Gaia EDR3 now enables its first measurement in the optical domain. Section 2 of Klioner et al. (2021) provides a richer historical overview tracing the evolution of our understanding of the solar system’s acceleration, from early theoretical insights to modern observational results. The reader is encouraged to consult it for additional context.

2.1 Overview of Gaia mission and Early Data Release 3 (EDR3)

In 2013, the European Space Agency’s (ESA) (see Prusti et al. (2016)), launched a space telescope under the Gaia mission (ended 27th of March 2025), with the main objective of scanning the sky to reproduce the most precise 3D map of the Milky Way. This was achieved by measuring the positions, distances, motions, and other properties of over a billion stars, transforming our understanding of Galactic structure, stellar kinematics and fundamental reference frames, highly important for the scope of this project.

Gaia EDR3 is a major data release from the ESA’s Gaia mission, published in December 2020. It includes improved astrometric and photometric data from nearly 1.8 billion sources, offering the most precise measurements of the positions, parallaxes, and proper motions. This served as a key step from DR2 to DR3, with significant advance in data quality and coverage.

2.2 Proper Motion & Reference Frame

Before delving into the details of proper motion, we need to recall the definition of aberration. In astronomy, aberration of light refers to the apparent displacement of celestial objects due to the motion of the observer through space. When the observer moves with a constant velocity, the apparent positions of stars shift in the direction of motion. However, if the observer’s velocity changes over time, i.e. if the observer is accelerating, this causes a time-dependent shift in apparent position. The result is an apparent pattern of systematic proper motions in the sky, mimicking a real motion of stars in the direction of the acceleration.

Aberration can be described in terms of the proper direction to the source, i.e. “the direction from which photons are seen to arrive, as measured in a physically adequate proper system of the observer” this appeared in section 3 of the paper titled *Gaia Early Data Release 3* (Klioner et al., 2021). Proper

direction is what we observe using astrometric tools in space, to describe it, we design the unit vector \mathbf{u} (Mignard & Klioner, 2012).

$$\mathbf{u} = \begin{pmatrix} \cos \alpha \cos \delta \\ \sin \alpha \cos \delta \\ \sin \delta \end{pmatrix} \quad (1)$$

The displacement $\delta\mu$, describes the aberration of light, determined by the proper directions of a source registered by two different observers that occupy the same position in space, but move at different velocities relative to each other, let the difference in velocities be \mathbf{v} . The Lorentz transforms relate the proper directions seen by the two co-located observers depending on \mathbf{v} . Due to the small differential effects that we are dealing with, first-order expression are sufficient, leading to first-order $|\mathbf{v}|/c$ (c denotes the speed of light), the proper direction is linear in \mathbf{v} .

$$\delta\mathbf{u} = \frac{\mathbf{v}}{c} - \frac{\mathbf{v} \cdot \mathbf{u}}{c} \mathbf{u} \quad (2)$$

“Equation 2 is accurate to $< 0.001\mu\text{as/yr}$ for $|\mathbf{v}| < 0.02\text{kms}^{-1}$, and to $< 1''$ for $|\mathbf{v}| < 600\text{kms}^{-1}$ ”, section 3 of Klioner et al. (2021). However, if \mathbf{v} is time dependent, $\delta\mathbf{u}$ inherits a similar dependency, systematically affecting all sources in the sky Klioner et al. (2021). The change with respect to time of proper direction, is the proper motion, i.e.

$$\frac{d(\delta\mathbf{u})}{dt} = \frac{\mathbf{a}}{c} - \frac{\mathbf{a} \cdot \mathbf{u}}{c} \mathbf{u} \quad (3)$$

where $\mathbf{a} = d\mathbf{v}/dt$ is the solar system barycentre acceleration with respect to the extragalactic source¹ Klioner et al. (2021). Proper motion², is the apparent angular motion³ of celestial objects across the sky, measured relative to more distant background stars or galaxies. Klioner et al. (2021) note that their Eq.(3) “has a global dipolar structure with axial symmetry along the acceleration: it is maximal for sources in the direction perpendicular to the acceleration and zero for directions along the acceleration”. Since one can only observe change in time and not the actual aberration, the reference frame related to equation (2) is irrelevant for our analysis. The velocity in equation (2) is dependent of the source, achieving larger or smaller aberration effects, however, this does not affect the proper motion in equation (3), this can be rewritten in the following form;

$$\mu = \mathbf{g} - (\mathbf{g} \cdot \mathbf{u})\mathbf{u} \quad (4)$$

where $\mu = d(\delta\mathbf{u})/dt$ is the proper motion vector and $\mathbf{g} = \mathbf{a}/c$ is also called the acceleration, in the context of this project, this might be expressed in terms of micro-arcsecond per year ($\mu\text{as yr}^{-1}$). We can rewrite Equation 4 in Cartesian components, as in Klioner et al., 2021, we obtain:

$$\begin{aligned} \mu_{\alpha*} &= -g_x \sin \alpha + g_y \cos \alpha \\ \mu_\delta &= -g_x \cos \alpha \sin \delta - g_y \sin \alpha \sin \delta + g_z \cos \delta \end{aligned} \quad (5)$$

where $\mu_{\alpha*} = \mu_\alpha \cos \delta$, and (g_x, g_y, g_z) are the components of the acceleration vector \mathbf{g} in the equatorial frame. These expressions directly relate the observer proper motion components to the solar system acceleration and the sources sky position. They form the basis for vector spherical harmonic (VSH), see Section 2.4, decomposition used in estimation process.

2.3 Theoretical Basis for Detecting Solar Acceleration

In Section 2.2, we derived the expected dipolar proper motion pattern induced by the solar system’s acceleration, expressed in vector and component forms (Equations 4 and 5). We now discuss its physical origin, focusing on theoretical expectations for the acceleration vector’s direction and magnitude from Galactic dynamics models. The acceleration components associated with the Galaxy’s large-scale structure are first described in Galactocentric cylindrical coordinates (R', ϕ', z') , with $z' = 0$ denoting the Galactic plane and the Sun located above it ($z' > 0$). These are then transformed into standard galactic coordinates (a_X, a_Y, a_Z) (Klioner et al., 2021).

¹in our case QSO-like or quasars

²not to be confused with parallax and proper velocity

³usually measured in arcsecond per year as/yr or milliarcseconds per year mas/yr

2.3.1 Expected Magnitude and Direction

The expected acceleration of the solar system barycentre can be inferred from the proper motion of Sagittarius A* (Sgr A*), the supermassive black hole at the Galactic centre. Because Sgr A* is assumed to be at rest in the Galactic frame, its observed proper motion primarily reflects the reflex motion of the Sun. Recent high-precision measurements give the Galactocentric distance as $d_{\text{GC}} = 8.178 \pm 0.013$ kpc (Abuter et al. (2019)), and the proper motion of Sgr A* in the Galactic plane as $\mu = 6.411 \pm 0.008$ mas yr⁻¹ (M. Reid and Brunthaler (2020)). To correct for the fact that the Sun is not exactly on a circular orbit, a velocity offset of 12.24 ± 0.2 km s⁻¹ is applied (Schönrich et al. (2010)). This results in an estimated centripetal acceleration of

$$a = 6.98 \pm 0.12 \text{ km s}^{-1} \text{ Myr}^{-1}, \quad (6)$$

which corresponds to a secular aberration drift of

$$\mu = \frac{a}{c} \approx 4.80 \pm 0.08 \text{ } \mu\text{as yr}^{-1}. \quad (7)$$

This value agrees well with estimates based on Galactic rotation models (e.g. M. Reid et al. (2014) and Malkin (2014)), and provides the benchmark against which Gaia’s astrometric data is compared (Klioner et al., 2021, Section 4.1).

2.3.2 Perturbation from Galactic and Extragalactic Structure

There are other ways to quantify the acceleration of the solar system; in this section we want to describe and report results from the acceleration towards the Galactic plane, since the Milky Way is a flattened system and the solar system is located marginally above the Galactic equator (Klioner et al., 2021). Additionally, we want to consider results from the acceleration arising from specific discrete sources, such as nearby galaxy clusters, Local Group members, giant molecular clouds, or individual nearby stars, Klioner et al., 2021.

Acceleration from non-axisymmetric components

The Milky Way is classified as a barred spiral galaxy⁴. Studies using Gaia DR2 (e.g., Katz et al. (2018); Abuter et al. (2019)) have shown that the Galactic bar and spiral arms significantly influence stellar velocities. In Klioner et al., 2021, the accelerations from the bar and spiral were analysed separately. Table 1 in Hunt et al. (2019) reviews various Galactic bar potential models; assuming the Sun lies 30° above the main bar axis (Wegg et al. (2015)), most models yield an acceleration of $0.04 \text{ km s}^{-1} \text{ Myr}^{-1}$ in the negative ϕ' direction, while the model by Pérez-Villegas et al. (2017) gives $0.09 \text{ km s}^{-1} \text{ Myr}^{-1}$. A recent study by Eilers et al., 2020 estimates a spiral-induced acceleration of $0.10 \text{ km s}^{-1} \text{ Myr}^{-1}$ along ϕ' , opposing the bar effect. This result is statistically robust but subject to systematic uncertainties from model assumptions, consistent with Monari et al. (2016) who report a systematic uncertainty of about $\pm 0.05 \text{ km s}^{-1} \text{ Myr}^{-1}$ (Klioner et al., 2021, Section 4.2).

Acceleration towards the Galactic plane

The Milky Way’s baryonic mass distribution is highly flattened, with a stellar disc axis ratio of roughly 1:10 and an even thinner gas disc composed of H_{II} and H_2 regions. The Sun lies slightly above the Galactic plane at $z \approx 25 \pm 5$ pc (Bland-Hawthorn and Gerhard, 2016). To estimate the vertical acceleration, Klioner et al., 2021 adopt the Galactic potential from McMillan (2016), which includes both stellar and gas components, yielding a downward acceleration of $0.15 \pm 0.03 \text{ km s}^{-1} \text{ Myr}^{-1}$. The earlier model by McMillan (2011), which omits gas discs, gives a slightly lower value of $0.12 \pm 0.02 \text{ km s}^{-1} \text{ Myr}^{-1}$, indicating that uncertainties from the potential are comparable to those from the Sun’s vertical position. In contrast, a geometric estimate based solely on the Sun’s offset gives a much smaller value of $\sim 0.02 \text{ km s}^{-1} \text{ Myr}^{-1}$. Combined, these yield acceleration components of $(-6.98 \pm 0.12, +0.06 \pm 0.05, -0.15 \pm 0.03) \text{ km s}^{-1} \text{ Myr}^{-1}$ (Klioner et al., 2021, Section 4.3).

Transformation to standard galactic coordinates

In Klioner et al., 2021, to compare model expectations with EDR3 observations, both were converted into standard Galactic coordinates (X, Y, Z) , which relate to Galactic longitude and latitude (l, b) . This

⁴A barred spiral galaxy features a central bar-shaped structure composed of stars extending from its nucleus.

system is defined via a transformation from the ICRS using three fixed angles (Sect. 1.5.3, Vol. 1 of ESA (1997)). Specifically, the Galactic equator’s north pole lies at ICRS coordinates ($\alpha = 192.85948^\circ, \delta = 27.12825^\circ$), and the origin of Galactic longitude is at the ascending node of the Galactic equator on the ICRS equator, $l_\Omega = 32.93192^\circ$. This defines the Galactic centre ($l = 0, b = 0$), corresponding to ICRS ($\alpha \approx 266.405^\circ, \delta \approx -28.936^\circ$). To convert the modelled acceleration into (a_X, a_Y, a_Z) , a small vertical-axis rotation of $10.5^\circ \pm 2'$ is applied to account for the Sun’s elevation, along with two axis sign flips, yielding

$$(a_X, a_Y, a_Z) = (-6.98 \pm 0.12, +0.06 \pm 0.05, -0.15 \pm 0.03) \text{ km s}^{-1} \text{ Myr}^{-1}. \quad (8)$$

The $2'$ uncertainty contributes only $\sim 0.004 \text{ km s}^{-1} \text{ Myr}^{-1}$ to a_Z , thus negligible. However, these transformations rely on idealised assumptions: the Galactic (X, Y, Z) system is treated as perfectly representing the true plane and barycentre, and the Galactic potential is assumed symmetric and flat. In reality, deviations of a few arcminutes can arise from structures like the bar and spiral arms. For instance, Sgr A*, expected at the potential minimum, is offset from the defined centre by about 3.3° in longitude and 2.7° in latitude — comparable to the 10.5° elevation from the Sun’s position. While current directional uncertainties are still a few degrees, these offsets become relevant as future measurements approach arcminute-level precision (Klioner et al., 2021, Section 4.4).

Specific objects

In addition to large-scale Galactic structures, small but non-negligible contributions to the solar system’s acceleration may arise from individual massive objects. These include nearby galaxies such as the Large Magellanic Cloud, giant molecular clouds within the Milky Way, or massive stellar associations. Whilst their combined effects is minor, typically well below $1 \text{ km s}^{-1} \text{ Myr}^{-1}$, they may introduce small anisotropies in the observed proper motion dipole. While negligible for current precision levels, they may become relevant in the future high-accuracy astrometric datasets (Klioner et al., 2021, Section 4.4).

2.3.3 Why Use Quasars?

A quasi-stellar object (QSO), or quasar, is a highly luminous active galactic nucleus (AGN) powered by accretion onto a supermassive black hole. Most massive galaxies are thought to host such black holes, with masses between 5×10^7 and $2 \times 10^9 M_\odot$ ⁵ (Burbidge and Perry (1976)). Infalling matter forms an accretion disk, where gravitational, viscous, and magnetic processes heat the gas, producing intense electromagnetic radiation across optical, ultraviolet, and X-ray wavelengths.

Quasars are ideal reference objects for measuring the solar system’s acceleration due to their extra-galactic distances and negligible intrinsic proper motions. Their apparent motions are unaffected by Galactic dynamics, allowing isolation of subtle systematic effects such as secular aberration drift. Unlike stars, which exhibit large proper motions from Galactic rotation and random velocities, quasars provide a stable inertial frame. Accordingly, the Gaia Celestial Reference Frame (Gaia-CRF3) is built using a large sample of quasars, ensuring minimal rotation. Thus, any systematic dipole pattern observed in their proper motions is interpreted as evidence for solar system barycentre acceleration (Klioner et al., 2021, Section 5.1).

2.4 Vector Spherical Harmonics (VSH) Framework

This section aims to provide a mathematical background and insights to VSH. Klioner et al. (2021) applied a VSH decomposition to the measured proper motion field of quasars to extract systematic patterns, including first order spheroidal components. These components corresponds to the glide, the global dipole signature expected from the secular aberration drift cause by the solar system’s acceleration.

2.4.1 Definition

VSH constitute an orthogonal set of basis functions for representing vector fields on the sphere. They are grouped into two distinct types: **toroidal** functions \mathbf{T}_{lm} and **spheroidal** functions \mathbf{S}_{lm} . In the physics literature, these are also commonly referred as ”magnetic” (or ”stream”) and ”electric” (or ”poloidal”/”potential”) components, respectively (Mignard and Klioner (2012), Section 2.1. Definition):

$$\mathbf{S}_{lm} = \frac{1}{\sqrt{l(l+1)}} r \nabla Y_{lm} = \mathbf{u} \times \mathbf{T}_{lm} \quad (9)$$

⁵ M_\odot denotes solar masses.

$$\mathbf{T}_{lm} = -\mathbf{u} \times \mathbf{S}_{lm} \quad (10)$$

where $\mathbf{u} = \mathbf{r}/r$ is the unit vector, see Equation 1, $|\mathbf{r}| = r$ is the radius-vector of the point and ∇ is the gradient operator. For any points on the surface of the unit sphere we have $r = 1$, furthermore for each l and m we have that $\mathbf{u} \cdot \mathbf{S}_{lm} = \mathbf{u} \cdot \mathbf{T}_{lm} = 0$ and $\mathbf{T}_{lm} \cdot \mathbf{S}_{lm} = 0$. One can define the basis vectors using the unit vector in Equation 1 for the toroidal and spheroidal components

$$\mathbf{e}_\alpha = \frac{1}{\cos \delta} \frac{\partial}{\partial \alpha} \mathbf{u} = \begin{pmatrix} -\sin \alpha \\ \cos \alpha \\ 0 \end{pmatrix}, \quad (11)$$

$$\mathbf{e}_\delta = \mathbf{u} \times \mathbf{e}_\alpha = \frac{\partial}{\partial \delta} \mathbf{u} = \begin{pmatrix} -\cos \alpha \sin \delta \\ -\sin \alpha \sin \delta \\ \cos \delta \end{pmatrix}, \quad (12)$$

Both \mathbf{e}_δ and \mathbf{e}_α are unit vectors, i.e. $|\mathbf{e}_\delta| = 1, |\mathbf{e}_\alpha| = 1$. Hence, the explicit formulas are for the toroidal and spheroidal functions are

$$\mathbf{T}_{lm}(\alpha, \delta) = \frac{1}{\sqrt{l(l+1)}} \left[\frac{\partial Y_{lm}}{\partial \delta} \mathbf{e}_\alpha - \frac{1}{\cos \delta} \frac{\partial Y_{lm}}{\partial \alpha} \mathbf{e}_\delta \right], \quad (13)$$

$$\mathbf{S}_{lm}(\alpha, \delta) = \frac{1}{\sqrt{l(l+1)}} \left[\frac{1}{\cos \delta} \frac{\partial Y_{lm}}{\partial \alpha} \mathbf{e}_\alpha + \frac{\partial Y_{lm}}{\partial \delta} \mathbf{e}_\delta \right], \quad (14)$$

Where Y_{lm} are the standard spherical functions, with the following choice of sign convention

$$Y_{lm}(\alpha, \delta) = (-1)^m \sqrt{\frac{2l+1}{4\pi} \frac{(l-m)!}{(l+m)!}} P_{lm}(\sin \delta) e^{im\alpha} \quad (15)$$

This holds for $m \geq 0$ ⁶, and for $m < 0$ we have

$$Y_{l,-m}(\alpha, \delta) = (-1)^m Y_{lm}^*(\alpha, \delta) \quad (16)$$

Where the complex conjugate of Y_{lm} is denoted as Y_{lm}^* , and P_{lm} is the associated Legendre functions, such that,

$$P_{lm}(x) = (1-x^2)^{\frac{m}{2}} \frac{d^m P_l(x)}{dx^m} \quad (17)$$

Where $P_l(x)$ is the Legendre polynomial. When we constructed the basis for our analysis, we did not use any existing Python packages for VSH functions, instead we decided to code everything from scratch, making our Python pipeline compatible with JAX, JAX allows the use of automatic differentiation. Another diversion from the Klioner et al. (2021) and Mignard and Klioner (2012), is that we defined Legendre polynomial, $P_l(x)$, using its binomial expansions

$$P_\ell(x) = \sum_{k=0}^{\lfloor \ell/2 \rfloor} \frac{(-1)^k}{2^\ell} \frac{(2\ell-2k)!}{k! (\ell-k)! (\ell-2k)!} x^{\ell-2k} \quad (18)$$

Notice that Equations 15 and 16 agree with the formula for the associated Legendre functions,

$$P_{l,-m}(x) = (-1)^m \frac{(l-m)!}{(l+1)!} P_{lm}(x) \quad (19)$$

The reader can find different conventions in the literature, particularly concerning the factor $(-1)^m$, however as stated in Mignard and Klioner (2012) Section 2.1, different conventions do not affect the vector spherical functions themselves.

Any smooth tangential vector field on the sphere, such as the observed proper motions of quasars, can be expanded in the VSH basis. As shown in Mignard and Klioner (2012), this expansion takes the form

$$\mu(\alpha, \delta) = \sum_{l=1}^{\infty} \sum_{m=-l}^l (t_{lm} \mathbf{T}_{lm}(\alpha, \delta) + s_{lm} \mathbf{S}_{lm}(\alpha, \delta)), \quad (20)$$

where t_{lm} and s_{lm} are the expansion coefficients corresponding to the toroidal and spheroidal modes, respectively. In our analysis, these coefficients were obtained by projecting the observed proper motion field onto the VSH basis defined in Equations 13 and 14.

⁶In our analysis we only considered this case, as there is not negative m values in the VSH expansion, see Eq. 21

3 Data & Preprocessing

The data used in this analysis were obtained from the [Gaia EDR3](#) via the Gaia Archive. We selected QSO-like objects identified in the [gaiadr3.agn_cross_id](#) table (more on quasars sample selection in [Section 3.1](#)), which lists sources matched to known active galactic nuclei (AGN). Astrometric and photometric parameters were retrieved using the [astroquery.gaia](#) Python package. The query joined the QSO identifiers with the [gaia_source](#) table to extract key quantities such as positions, proper motions, parallaxes, errors, and quality indicators (e.g. RUWE). The exact ADQL query used is listed below:

```

1 SELECT
2   agn.source_id,
3   gs.ra, gs.dec,
4   gs.pmra, gs.pmdec,
5   gs.parallax, gs.parallax_error,
6   gs.ruwe, gs.phot_g_mean_mag,
7   gs.nu_eff_used_in_astrometry,
8   gs.pmra_error,
9   gs.pmdec_error,
10  gs.pmra_pmdec_corr,
11  gs.astrometric_params_solved
12 FROM gaiadr3.agn_cross_id AS agn
13 JOIN gaiadr3.gaia_source AS gs
14 ON agn.source_id = gs.source_id

```

The resulting table was downloaded programmatically and saved as a CSV file for further preprocessing (see full script in [src/data/data_download.py](#)).

3.1 QSO Sample Selection

The full Gaia EDR3 dataset provides high-accuracy astrometry for over 1.5 billion sources, most of which are stars. However, there is evidence that a subset of a few million sources are quasars and other extragalactic objects dense enough for Gaia to obtain accurate astrometric solutions. Since Gaia EDR3 lacks purely internal astrophysical classification, QSO-like sources were identified via cross-matching with 17 external QSO and AGN catalogues. To ensure high-quality astrometry, sources with proper motions consistent with zero within five times their formal uncertainties were retained, reducing stellar contamination but potentially excluding some genuine QSOs. This filtering does not impact the detection of the systematic solar acceleration signal, which is two orders of magnitude smaller. Further quality checks were applied, resulting in a catalogue of 1,614,173 QSO-like sources, published in Gaia EDR3 as table [agn_cross_id](#). A detailed description of this procedure and Gaia-CRF3 construction is forthcoming (Gaia Collaboration, in prep.).

Gaia EDR3 provides three astrometric solution types (Lindgren et al., 2021): (i) two-parameter solutions (position only), (ii) five-parameter solutions (position, parallax, proper motion), and (iii) six-parameter solutions, which include an estimate of the effective wavenumber ν_{eff} (pseudo-colour). The effective wavenumber represents the flux-weighted inverse wavelength over Gaia’s G-band and relates to the colour index $G_{\text{BP}} - G_{\text{RP}}$, with approximate conversions given in Lindgren et al. (2021): ν_{eff} values of 1.3, 1.6, and 1.9 μm^{-1} correspond to colour indices of about 2.4, 0.6, and 0.5, respectively (Klioner et al., 2021, Section 5.1).

Due to astrometric filtering during Gaia-CRF3 construction, all selected sources have either five- or six-parameter solutions. Specifically, the sample comprises 1,215,942 sources with five-parameter and 398,231 with six-parameter solutions (Klioner et al., 2021, Section 5.1, Table 1). On average, six-parameter sources are fainter, redder, and exhibit slightly lower astrometric quality, as indicated by their renormalised unit weight error (RUWE). Independent studies (e.g., Fabricius et al., 2021; Lindgren et al., 2021) have shown that five-parameter solutions generally have smaller systematic errors, especially for $G > 16$, which applies to most QSO-like sources. Therefore, our analysis focuses on the 1,215,942 Gaia-CRF3 sources with five-parameter solutions (Klioner et al., 2021, Section 5.1).

3.2 Filtering and Quality Cuts

We successfully reproduced Figures 1-3, (compare these plots with Klioner et al., 2021, Section 5.1, Figures 3-5). See Jupyter notebook [plots.ipynb](#). However, the only plots that are visually different are

Figure 4 and Figure 6, in Section 5.1, Klioner et al. (2021), this is due to scaling, we chose not to apply logarithmic scaling, resulting in visually different plots, but they essentially deliver the same message, see below. To produce these plots we first had to separate the five and six-parameters solutions in the dataset. We used `Pandas` to load the dataset and its module `DataFrame` to read and manage it.

```

1 import pandas as pd
2 df = pd.read_csv("csv_files/qso_full_data.csv")
3 df_5param = df[df["astrometric_params_solved"]==31]
4 df_6param = df[df["astrometric_params_solved"]==95]

```

The column `astrometric_params_solved` indicates the type of astrometric solution provided for each source. Vales of 31 correspond to five-parameter solutions, which include position, parallax, and proper motion, while values of 95 denote six-parameter solutions, which additionally include a pseudo-colour estimate. For the purposes of our analysis we retained only the five-parameter solutions, consistent with the quality requirements used in the construction of the Gaia-CRF3 catalogue.

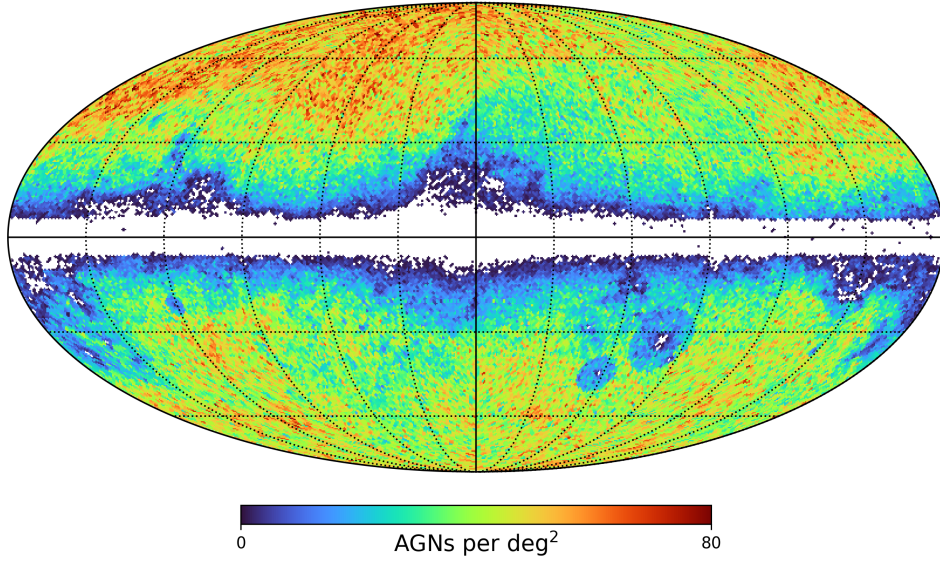


Figure 1: Sky distribution of Gaia-CRF3 QSO-like sources in Galactic coordinates, shown as source density per square degree using HEALPix binning ($N_{\text{side}} = 64$). The density is computed from the five-parameter subset of the Gaia EDR3 AGN catalogue. Regions near the Galactic plane are masked or show low source density due to strong extinction and stellar contamination. The map uses a Mollweide projection with a linear colour scale ranging from 0 to 80 AGNs per deg².

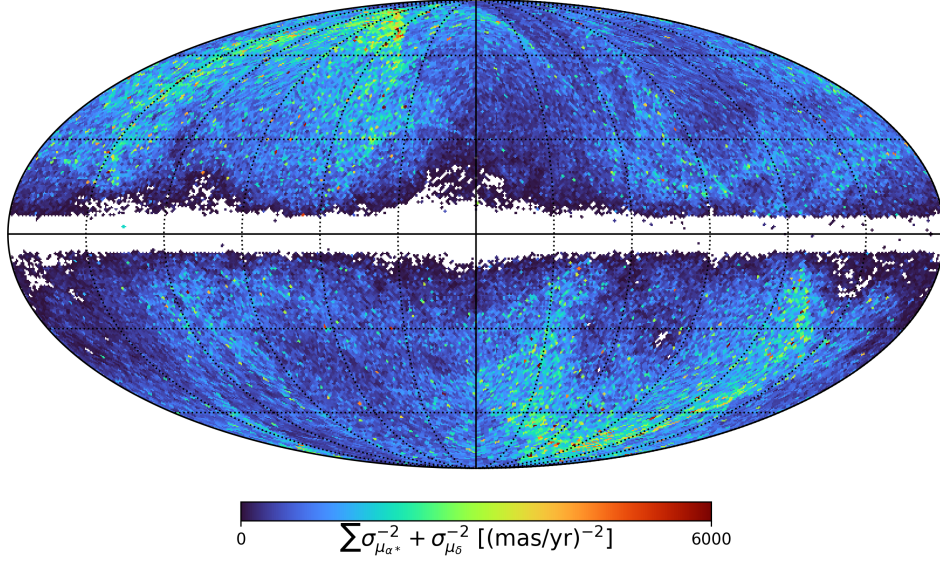


Figure 2: Sky distribution of the statistical weights used in the proper motion analysis, shown in Galactic coordinates with HEALPix binning ($N_{\text{side}} = 64$). Each pixel shows the sum of inverse squared uncertainties in proper motion, $\sigma_{\mu_{\alpha^*}}^{-2} + \sigma_{\mu_{\delta}}^{-2}$, for all sources in that pixel. Brighter regions correspond to areas with the higher astrometric precision and/or more sources. The white band near the Galactic plane reflects masked or excluded regions due to high stellar contamination or astrometric uncertainty.

As outlined in Sections 5 and 6 of Klioner et al. (2021), their estimation of the solar system’s acceleration relies on expanding the vector field of proper motions into orthogonal functions on the sphere (see Section 2.4). While a homogeneous sky distribution of data points is desirable, Section 7.3 of Mignard and Klioner (2012) emphasizes that dynamical homogeneity—i.e., the distribution of statistical weights reflecting astrometric precision—is more critical than purely kinematic homogeneity. This weighted distribution is shown in Figure 2 (Klioner et al., 2021, Section 5.1).

A clean sample of QSO-like sources is essential to avoid systematic biases from stellar contamination. Histograms of normalised parallaxes and proper motions (Figure 4) provide a diagnostic: for a genuine extragalactic sample, these distributions should be Gaussian with zero mean and unit standard deviation. Given typical proper motion uncertainties exceeding $400 \mu\text{as yr}^{-1}$ (Klioner et al., 2021, Section 4.5, Table 1), the subtle effect of solar acceleration is negligible here. The red curves in Figure 4 show best-fit Gaussians, closely matching the data. The fitted standard deviations are 1.052 for parallaxes, 1.055 for proper motions in right ascension, and 1.063 in declination, consistent with Klioner et al. (2021). The Gaussian fits were performed using the Python package `scipy.stats.norm`, providing best-fit means and standard deviations to validate sample purity and error consistency. The close agreement justifies assuming Gaussian measurement errors in our subsequent analysis (Klioner et al., 2021, end of Section 5.1).

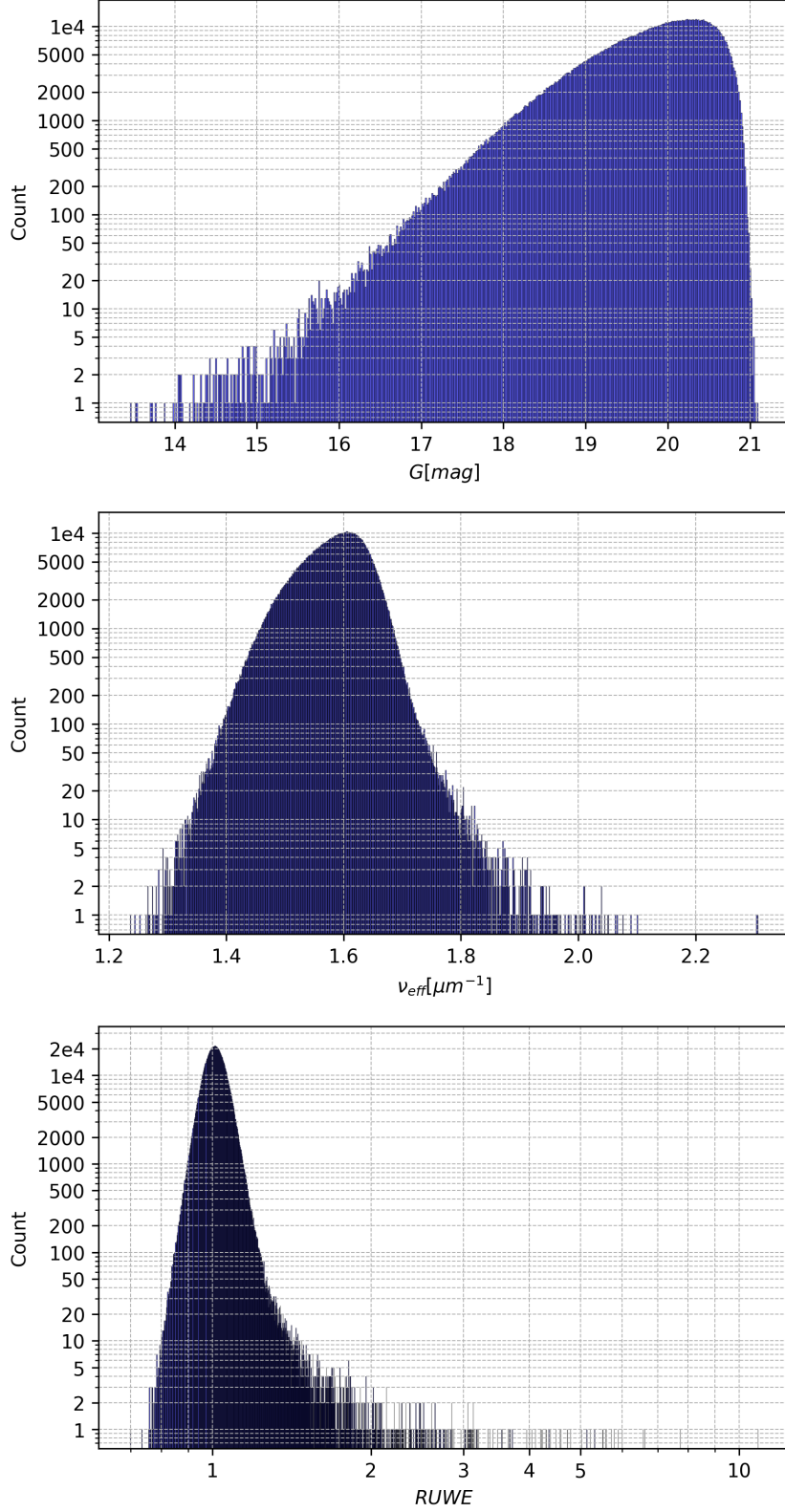


Figure 3: Distributions of key astrometric parameters for the Gaia-CRF3 sources with five-parameter solutions: G-band magnitude (top), effective wavenumber ν_{eff} (middle), and RUWE (bottom). All distributions are shown on logarithmic scale highlight tails and outliers. These properties inform both astrometric quality and filtering decisions in the analysis.

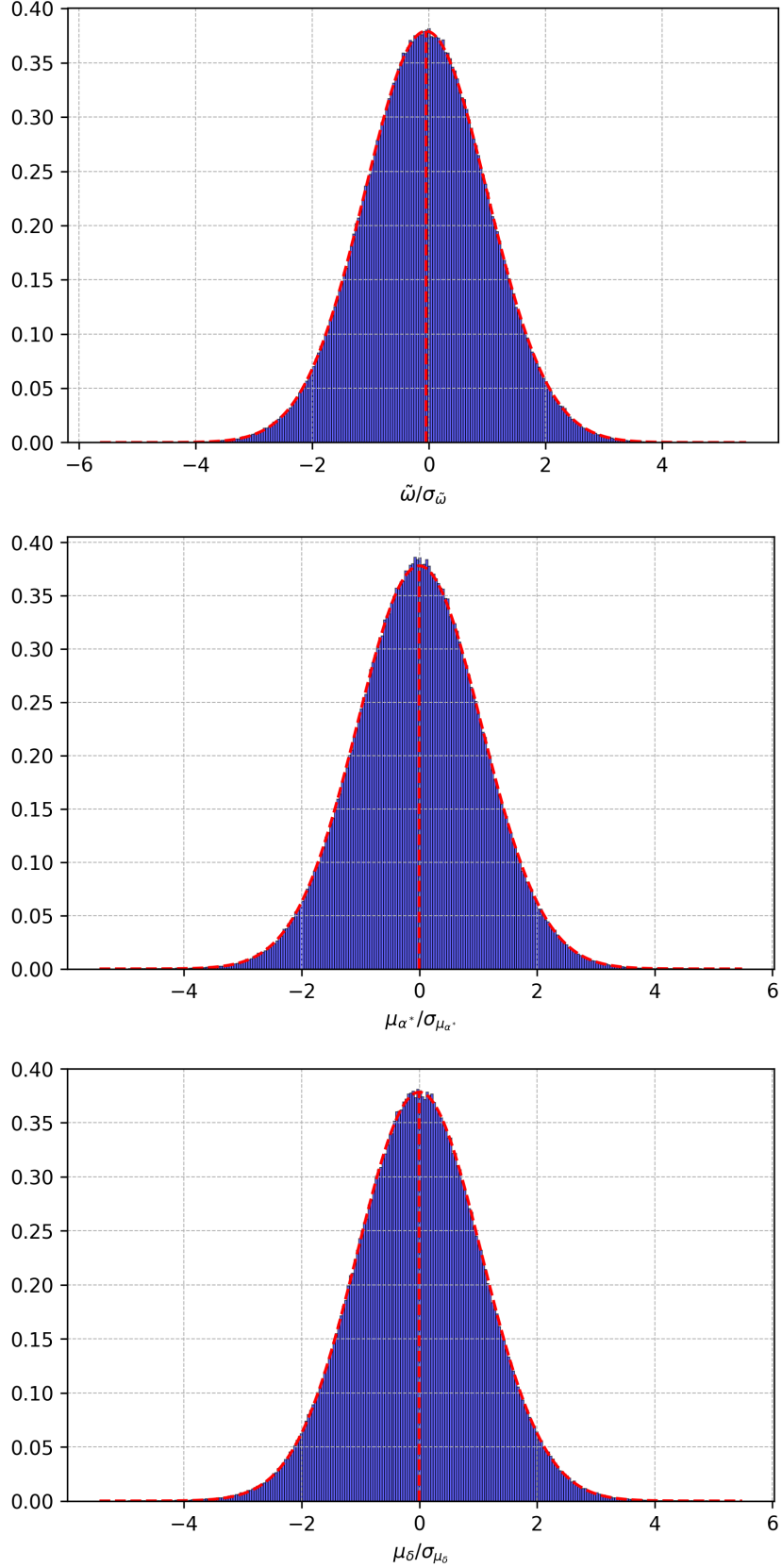


Figure 4: Distributions of normalised astrometric quantities for Gaia-CRF3 sources with five-parameter solutions: parallax (top), proper motion in RA μ_{α^*} (middle), and proper motion in declination μ_{δ} (bottom), each divided by their formal uncertainty. These distributions are expected to approximate standard normal distributions if the uncertainties are well estimated and the sources have negligible true values, as expected for distant quasars.

3.3 Galactic Object

In this section, we discuss why Galactic objects are not used to determine the solar system’s acceleration (see Klioner et al., 2021, Section 5.2). The expected proper motion signature from solar acceleration is approximately $5 \mu\text{as yr}^{-1}$ (Equation 7), which is dwarfed by typical Galactic kinematic effects, such as rotation and shear, at 5–10 mas yr^{-1} —over a thousand times larger. Although the classical Oort model does not introduce a glide component, apparent glide-like patterns can arise from mismatches between the Sun’s motion and the mean motion of specific stellar populations.

Notable examples include the Sun’s motion toward the apex in Hercules (near $l = 270^\circ, b = 30^\circ$) and the asymmetric drift of older stars (toward $l = 318^\circ, b = 48^\circ$). These directions are only $\sim 40^\circ$ apart, so their combined influence forms a substantial large-scale pattern. Moreover, these effects depend on distance and, for asymmetric drift, also on stellar age. At about 1 kpc, these motions become comparable to Oort terms, far exceeding the subtle acceleration-induced drift.

Even small deviations from axisymmetric Galactic rotation, such as slight second derivatives in the rotation curve, can generate glide-like signatures. Further distortions arise from local stellar streams, the Galactic bar, and spiral arms. Due to the overwhelming amplitude and complexity of these motions, isolating the $5 \mu\text{as yr}^{-1}$ acceleration signal is impractical. This is why extragalactic sources are used, as they remain unaffected by local Galactic kinematics (Klioner et al., 2021, Section 5.2).

4 Methods

We based our method on determining parameter estimates for the acceleration components described in Section 2, followed the footsteps of Klioner et al. (2021), described in their Section 6 (Methods). In which they mentioned that there are many potential approaches to estimate the acceleration from observed proper motions. One straightforward method would be to perform a least-square fit of proper motion components using Equation 5 to solve directly for the acceleration vector. However, this approach becomes problematic in the presence of other large-scale patterns in the data, such as global rotation. These additional signals can introduce bias into the acceleration estimate, especially because they are generally not orthogonal to the acceleration-induced dipole when accounting for non-uniform statistical weight distribution across the sky (see Figure 2). Instead one can use VSH for a give set of sources, allowing a reduction of biases present in large scale patterns, providing a superior control over systematic errors. We want to perform a fit on the real-valued expansion of Equation 20, this is defined as

$$\boldsymbol{\mu}(\alpha, \delta) = \sum_{l=1}^{l_{\max}} \left(t_{l0} \mathbf{T}_{l0} + s_{l0} \mathbf{S}_{l0} + 2 \sum_{m=1}^l (t_{lm}^{\Re} \mathbf{T}_{lm}^{\Re} - t_{lm}^{\Im} \mathbf{T}_{lm}^{\Im} + s_{lm}^{\Re} \mathbf{S}_{lm}^{\Re} - s_{lm}^{\Im} \mathbf{S}_{lm}^{\Im}) \right), \quad (21)$$

where the superscripts \Re and \Im denote the real and imaginary parts respectively, for each complex quantity. Equation 21 is defined as `model_vsh` in `src/models/vsh_model`, just like all the other functions in Section 2.4, we built everything using JAX, which is also compatible with NumPyro (See Section 5). Our analysis objective is to find the parameter estimates for the VSH coefficients in Equation 21, these are t_{lm} and s_{lm} , these estimates are used determine the solar system’s acceleration. A useful resource of the VSH formalism is that the degree $l = 1$ harmonics have a direct physical interpretation: the toroidal components T_{1m} correspond to a global rotation to the reference frame, while the spheroidal components S_{1m} describe the glide pattern. Notably, this glide term shares the same mathematical structure as the acceleration-induced proper motion described in Equation 5. As shown in Section 4.2 of Mignard and Klioner (2012), this correspondence can be formally demonstrated as:

$$\begin{aligned} s_{10} &= \sqrt{\frac{8\pi}{3}} g_z, \\ s_{11}^{\Re} &= -\sqrt{\frac{4\pi}{3}} g_x, \\ s_{11}^{\Im} &= \sqrt{\frac{4\pi}{3}} g_y. \end{aligned} \quad (22)$$

These relations show how the acceleration vector components g_x, g_y and g_z map directly onto the degree $l = 1$ spheroidal VSH coefficients. This makes it possible, in principle, to estimate the solar system’s acceleration using a minimal model with only $l = 1$. However, as noted earlier, higher-order harmonics are essential to absorb residual large-scale systematics and other proper motion patterns not related to

the acceleration itself. Including these higher-order terms helps to isolate the true dipole signal from potential contaminations (Klioner et al., 2021, Section 6). The VSH T_{lm} and S_{lm} form an orthonormal and complete basis for vector fields on the S^2 , under the L^2 norm. As with scalar spherical harmonics, higher l corresponds to finer spatial structure. However, orthogonality between modes assumes an infinite, homogeneous distribution of data points. In practice, with a finite, unevenly distributed dataset, VSH modes are not strictly orthogonal, and correlation depends on the sky distribution of the statistical weights (see Figure 2). For the dataset used in this study, numerical tests show that limiting the expansion to $l_{\max} \leq 10$ keeps parameter correlations below ~ 0.6 , ensuring a stable fit. Projecting the model onto the local basis vectors yields two equations per source, leading $2k$ observations for $2l_{\max}(l_{\max} + 2)$ unknowns, which are solved using weighted least squares, Equation 23 (used in Klioner et al. (2021), see Sections 6 & 7). The weights account for proper motion uncertainties, and it is beneficial to include the published correlation between μ_{α^*} and μ_{δ} for each source. Correlations between different sources, however are not accounted for this analysis.

$$\begin{aligned} X^2 &= [\Delta\mu_{\alpha^*} \quad \Delta\mu_{\delta}] \begin{bmatrix} \sigma_{\mu_{\alpha^*}}^2 & \rho_{\mu} \sigma_{\mu_{\alpha^*}} \sigma_{\mu_{\delta}} \\ \rho_{\mu} \sigma_{\mu_{\alpha^*}} \sigma_{\mu_{\delta}} & \sigma_{\mu_{\delta}}^2 \end{bmatrix} \begin{bmatrix} \Delta\mu_{\alpha^*} \\ \Delta\mu_{\delta} \end{bmatrix} \\ &= \frac{1}{1 - \rho_{\mu}^2} \left[\left(\frac{\Delta\mu_{\alpha^*}}{\sigma_{\mu_{\alpha^*}}} \right)^2 - 2\rho_{\mu} \left(\frac{\Delta\mu_{\alpha^*}}{\sigma_{\mu_{\alpha^*}}} \right) \left(\frac{\Delta\mu_{\delta}}{\sigma_{\mu_{\delta}}} \right) + \left(\frac{\Delta\mu_{\delta}}{\sigma_{\mu_{\delta}}} \right)^2 \right] \end{aligned} \quad (23)$$

The angular distribution of the detected signal is also consistent with the expected dipolar pattern induced by acceleration (see Eq. (8) in Klioner et al., 2021), though this is not explored in detail here.

4.1 Frequentist Approach

In Klioner et al. (2021), Section 6 & 7, they described their methodology to determine the VSH coefficient estimates. Their approach is purely frequentist, using Equation 23 to perform a weighted least square fit for different values of l_{\max} , and then used 550 000 bootstrapping experiment to determine each estimate uncertainties. Furthermore, they performed outlier detection (Algorithm 1) implemented in Lindegren et al. (2018).

Algorithm 1 Iterative Outlier Rejection

- 1: Initial Least-Squares Fit ▷ Fit the VSH model using all data
 - 2: **repeat**
 - 3: Compute X^2 values ▷ For each QSO
 - 4: Compute median of X values
 - 5: **for all** sources **do**
 - 6: **if** $X > \kappa \times \text{median}(X)$ **then**
 - 7: Mark as outlier
 - 8: **end if**
 - 9: **end for**
 - 10: Refit model excluding outliers
 - 11: **until** outlier set no longer changes
-

4.2 Bayesian Approach

We decided to base our analysis on the Bayesian framework, we adopted the same outlier rejection in Klioner et al. (2021) (Algorithm 1), allowing us to work with a similar dataset size after outlier rejection, to ensure reproducibility. We relied on Hamiltonian Monte Carlo (HMC) algorithm to determine both estimates and uncertainties of the VSH coefficients. Bayesian inference is the process of determining posterior distributions by combining a likelihood function, a prior distribution (which reflects our prior knowledge), and the evidence⁷.

$$P(\theta | D) = \frac{\mathcal{L}(D | \theta) \pi(\theta)}{Z} \quad (24)$$

Bayes' theorem is shown in Equation 24, where:

⁷A normalising constant that ensures the posterior is a valid probability distribution

- θ are the model parameters, and D is the observed data.
- $P(\theta | D)$ is the posterior distribution, the quantity of interest.
- $\mathcal{L}(D | \theta)$ is the likelihood function, representing the probability of the data given the parameters.
- $\pi(\theta)$ is the prior, encoding beliefs about θ before observing the data.
- Z is the evidence, a normalising constant computed by integrating the likelihood times the prior over the entire parameter space.

To approximate the posterior distribution, one can use dedicated sampling algorithms such as HMC. These methods generate samples from the posterior by efficiently exploring parameter space, guided by both the likelihood and the prior. In our case, HMC leverages gradient information from the log-posterior to produce samples that accurately reflect the combined influence of the prior and likelihood specified in the model.

4.2.1 Choice of Prior

Our choice of prior is a standard normal distribution, a Gaussian with mean zero and standard deviation $\sigma = 1$. This is a natural choice, as the VSH coefficients can be either positive or negative. The standard deviation is expressed in units of mas yr^{-1} , which allows the prior to cover a broad range of physically plausible values. In particular, it comfortably spans the expected scale of the VSH coefficients, which typically range from a few tens to several hundred $\mu\text{as yr}^{-1}$ (i.e., up to $\sim 0.5 \text{ mas yr}^{-1}$).

Choosing a standard normal prior also brings computational advantages: it simplifies implementation, encourages numerical stability, and integrates well with gradient-based samplers like HMC. Additionally, it acts as a weakly informative prior, helping regularise the solution without imposing strong biases.

Additionally, as a side check, we repeated one of our experiments with a uniform prior in range $[-1, 1]$, this also allows a wide search in the parameter space. This did not impact our final results, for VSH coefficient estimates, however we observed negligible changes in our overall solar system’s acceleration uncertainty. This indicates that the data are sufficiently informative and that our results are robust to prior assumptions.

4.2.2 Likelihood Function

We chose a Gaussian log-likelihood, proportional to $\log \mathcal{L} \sim -\frac{1}{2}X^2$ (X^2 is defined in Equation 23), which assumes that the astrometric residuals are independently normally distributed with known uncertainties. This choice is standard in astrometric modelling, aligns with the error assumptions in the Gaia catalogue, and corresponds to the log-likelihood for a multivariate Gaussian. It also ensures compatibility with HMC, which benefits from smooth, differentiable objective functions.

5 Analysis & Results

This section aims to present the results achieved with our analysis and compare them with the results in Klioner et al. (2021). We followed the same procedure for all plots shown in this section. The HMC sampling algorithm was run across multiple chains (either 6 or 8 for the main analysis, i.e. $l_{\max} = 3$), each with 2000 warm-up steps (burn-in) and 5000 samples. After discarding the burn-in, we associated convergence using the \hat{r} diagnostic⁸; if $\hat{r} \approx 1.0$ for each parameter across all chains, we considered the sampling to have converged. To reduce autocorrelation in the posterior samples of the VSH coefficients of interest, i.e. s_{10} , $s_{11}^{\mathfrak{R}}$ and $s_{11}^{\mathfrak{I}}$, we estimated the integrated autocorrelation time (IAT) and applied the thinning accordingly. To determine the VSH coefficient estimates and their associated uncertainties, we computed the mean and standard deviation of the posterior samples for each parameter. It is important to note that the number of VSH coefficients depends on the chosen value of l_{\max} . Specifically, the number of coefficients is given by:

$$\text{Number of coefficients} = 2 \cdot l_{\max}(l_{\max} + 2) \quad (25)$$

This includes both the toroidal and spheroidal components up to degree l_{\max} . As l_{\max} increases, the number of VSH coefficients grows quadratically, making the analysis increasingly computationally demanding.

⁸Also known as the Gelman-Rubin statistic, \hat{r} compares the variance between chains to the variance within chains. Values close to 1.0 indicate convergence.

In Figure 5, we show the three components of the glide vector as a function of l_{\max} for the different proper motions of the 1 215 942 Gaia-CRF3 sources with five-parameter solutions. The results are displayed in both equatorial and galactic coordinate systems. The equatorial components were obtained using Equation 22, which converts the VSH coefficients ($s_{10}, s_{11}^{\Re}, s_{11}^{\Im}$) [mas yr^{-1}] to the corresponding equatorial glide components (g_x, g_y, g_z) [$\mu\text{as yr}^{-1}$].

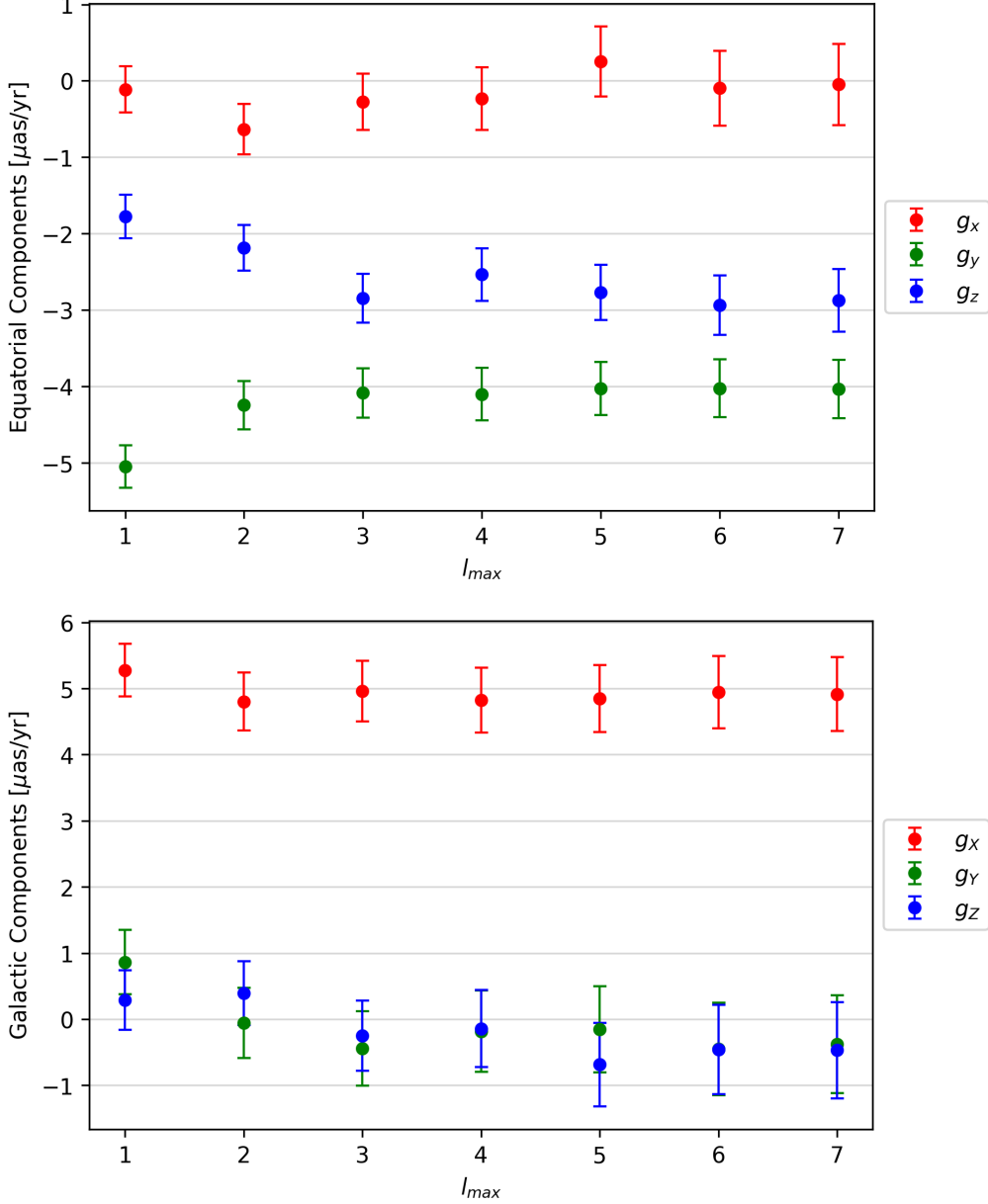


Figure 5: Equatorial (top figure) and galactic (bottom figure) components of the solar system acceleration as a function of l_{\max} . The error bars are with in $\pm 1\sigma$ uncertainty. Compare with Figure 7, Section 7 of Klioner et al., 2021. It is important to notice that outlier detection was performed Figure 7 of Klioner et al. (2021), and they rejected ~ 3800 per l_{\max} , however we did not remove any outliers to produce this plot.

The galactic components (g_X, g_Y, g_Z) were computed by rotating the equatorial glide vector and its associated covariance matrix into the galactic reference frame. One can observe that for $l_{\max} \geq 3$, the estimated components of the glide vector become stable, with differences between successive values remaining well within their respective uncertainties. The noticeable deviation at lower values of l_{\max} indicates that higher order systematics in the data must be accounted for, although their impact on the glide estimate appears relatively minor. Based on this, we adopt the results at $l_{\max} = 3$ as our final

estimates for the acceleration components. For $l_{\max} = 3$, the model involves estimating 30 parameters, which offers an effective trade-off between computational efficiency and the robustness of the inferred results.

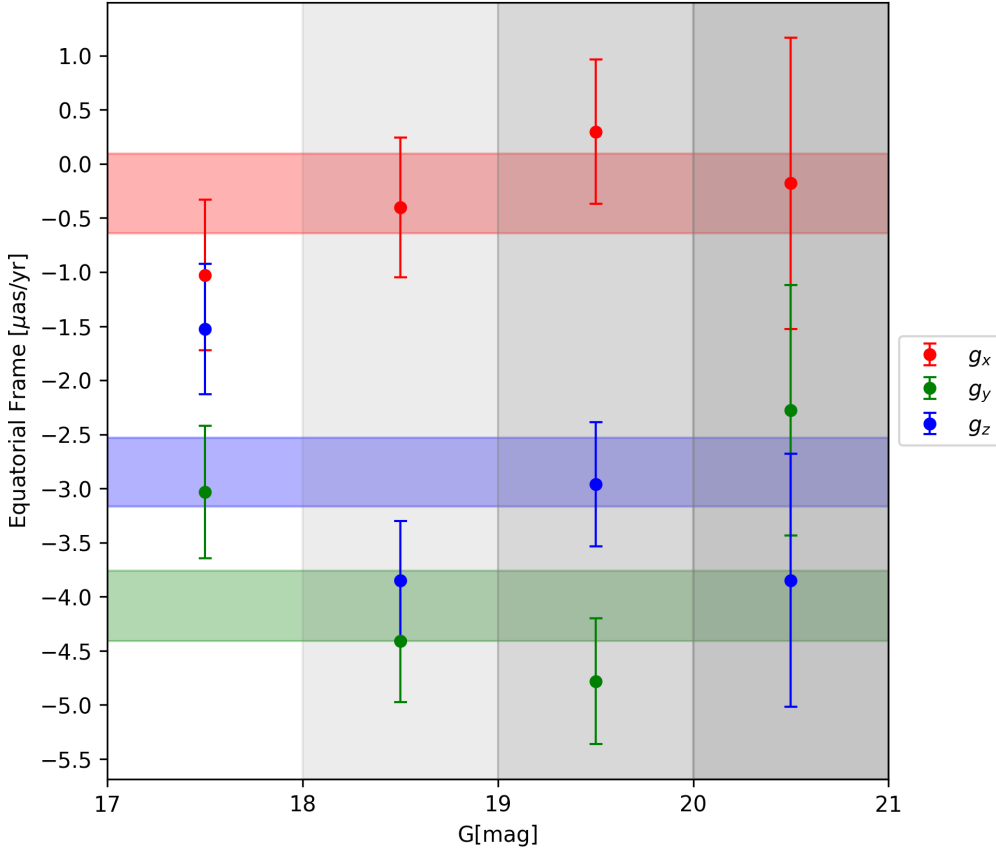


Figure 6: Equatorial components of the acceleration vector (g_x, g_y, g_z) estimated from QSO-like sources binned by Gaia G -band magnitude: $G \leq 18$ (29 200 sources), $18 < G \leq 19$ (146 614 sources), $19 < G \leq 20$ (490 161 sources), and $G > 20$ (549 967 sources). Error bars represent 1σ uncertainties from posterior sampling in each bin. The shaded horizontal bands indicate the values and associated uncertainties ($\pm 1\sigma$, the height corresponds to twice the uncertainty) for each component derived from the full dataset, independent of magnitude. This comparison illustrates the stability of the acceleration signal across different magnitude ranges.

Systematic errors in Gaia EDR3 astrometry are known to correlate with both the magnitude and colour of observed sources (Lindgren et al., 2021). To assess the impact of these dependencies on the acceleration estimates, we performed HMC sampling using $l_{\max} = 3$ on subsets of the data divided by G -band magnitude and by colour, the latter being represented by the effective wavenumber ν_{eff} . Figure 6 shows the estimated acceleration components across different G -magnitude intervals. The variations are relatively small, and the results remain consistent with those derived from the full dataset. A similar analysis based on colour is presented in Figure 7. Again, the component estimates across colour bins closely match the full-sample values, confirming the robustness of the result against these known systematics (Klioner et al. (2021), Section 7). Systematic effects in Gaia DR ℓ astrometry are known to depend on both magnitude and colour. However, since bluer QSO-like sources tend to be fainter, the two selection criteria are not entirely independent. Additionally, colour and magnitude cuts result in less uniform sky coverage compared to the full sample, due in part to Galactic extinction and reddening. Despite these limitations, we find that any resulting bias in the acceleration estimates is smaller than the formal uncertainties from the full dataset.

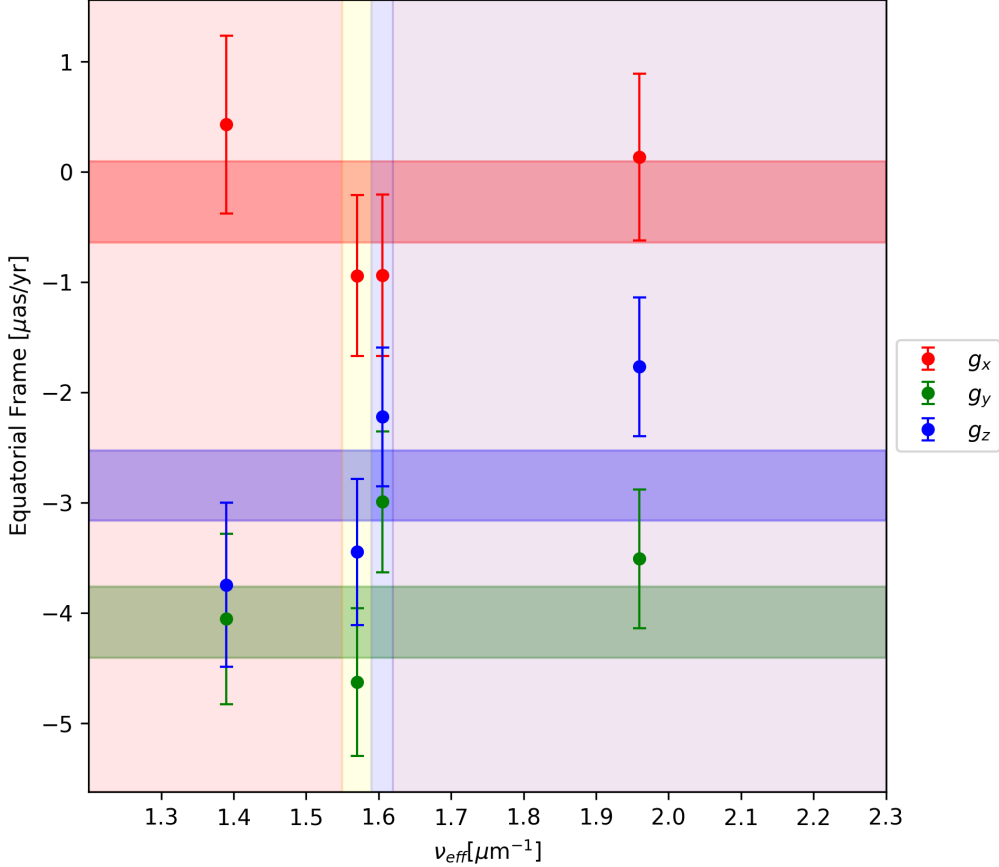


Figure 7: Equatorial components of the associated acceleration vector along with their associated uncertainties, shown across four intervals of the effective wavenumber ν_{eff} , distribution in the selected dataset, ensuring each bin contains $\sim 304\,000$ sources. The shaded horizontal bands represents the values and uncertainties (with width equal to twice the uncertainty) computed from the full sample, serving as a reference for comparison.

Another potential source of bias is charge transfer inefficiency (CTI) in the CCD detectors. Simulations of plausible CTI-related effects not corrected in Gaia DR3 show that their impact on the estimated glide is minimal, at most $\sim 0.1 \mu\text{as yr}^{-1}$, well below the quoted uncertainty.

Stellar contamination is also a concern. Even a small number of misidentified stars, especially those with larger intrinsic proper motions, could bias the acceleration estimate. While the outlier rejection procedure used in the VSH fit (Algorithm 1) helps mitigate this, a more direct check was performed using control sample: source selected identically to the QSO-like set, but without cross-matching to external AGN catalogues. Applying the VSH method to this sample of 23.6 million sources (mostly stars) yields a large glide ($\sim 360 \mu\text{as yr}^{-1}$) in the direction opposite the Sun’s motion. This direction is nearly orthogonal to the glide measured from the QSO-like sample, implying that any residual stellar contamination may affect the direction slightly, but not the magnitude of the acceleration. We find no such directional bias and conclude that the effect is negligible (Klioner et al., 2021, Section 7). Another potential source of systematic bias is error in Gaia’s barycentric ephemeris, which defines the reference frame used in the astrometric solution. Systematic acceleration in the ephemeris over the mission duration could mimic a real acceleration signal. However, Klioner et al. (2021) show that such errors, based on comparisons between planetary ephemerides (e.g. INPOP10e vs. INPOP19a), are at least two orders of magnitude smaller than the measured signal, and thus negligible at the current precision level.

5.1 Summary of Results

Having described the above considerations, for our final analysis we performed outlier detection, Algorithm 1, with $\kappa = 3$ and rejected 3785 source, after 6 iterations of the algorithm. We then used HMC sampling on the filtered dataset to determine the posterior distributions of the VSH coefficients, with

2 000 warm-ups, 5 000 samples, across 8 chains. After performing convergence checks mentioned above, we determined a IAT value of 2, and performed sample thinning accordingly, hence we were left with a sample size of 20 000, which is more than sufficient for our analysis. Results are shown in Table 1.

Table 1: Final estimate of the Solar System acceleration vector. All the uncertainties are with in $\pm 1\sigma$, these are obtained from HMC sampling.

Quantity	Value	Uncertainty
<i>Equatorial components</i>		
g_x [$\mu\text{as yr}^{-1}$]	−0.08	0.45
g_y [$\mu\text{as yr}^{-1}$]	−4.30	0.37
g_z [$\mu\text{as yr}^{-1}$]	−2.65	0.23
α [deg]	268.97	6.05
δ [deg]	−31.62	3.11
<i>Correlations</i>		
ρ_{g_x, g_y}	−0.092	
ρ_{g_x, g_z}	+0.020	
ρ_{g_y, g_z}	+0.001	
$\rho_{\alpha, \delta}$	+0.042	
<i>Galactic components</i>		
g_X [$\mu\text{as yr}^{-1}$]	+5.04	0.34
g_Y [$\mu\text{as yr}^{-1}$]	−0.10	0.34
g_Z [$\mu\text{as yr}^{-1}$]	−0.29	0.40
l [deg]	358.82	3.87
b [deg]	−3.28	4.61
<i>Correlations</i>		
ρ_{g_X, g_Y}	+0.307	
ρ_{g_X, g_Z}	+0.081	
ρ_{g_Y, g_Z}	−0.466	
$\rho_{l, b}$	−0.008	
$ \mathbf{g} $ [$\mu\text{as yr}^{-1}$]	5.05	0.34

We present the posterior distribution of the equatorial coordinates (RA,Dec) corresponding to the inferred direction fo the solar system' acceleration. The results shown in Figure 8 as a corner plot, with the median values and 68% credible intervals, given by:

$$\text{RA} = 268.98^{+4.96}_{-4.93} \text{ deg}, \text{ Dec} = -31.49^{+3.57}_{-3.69} \text{ deg}$$

For reference, the known position of the Galactic Centre (Sgr A*) is located at:

$$\text{RA}_{\text{GC}} = 266.42^\circ, \text{ Dec}_{\text{GC}} = -29.01^\circ$$

The red cross in the 2D posterior panel marks this true location. The Galactic Centre lies well within the high-density region of the inferred posterior, indicating that our recovered acceleration direction is statistically consistent with the expected direction towards the Galactic Centre. This result supports the detection of the secular aberration drift due to the solar system's acceleration within the Milky Way.

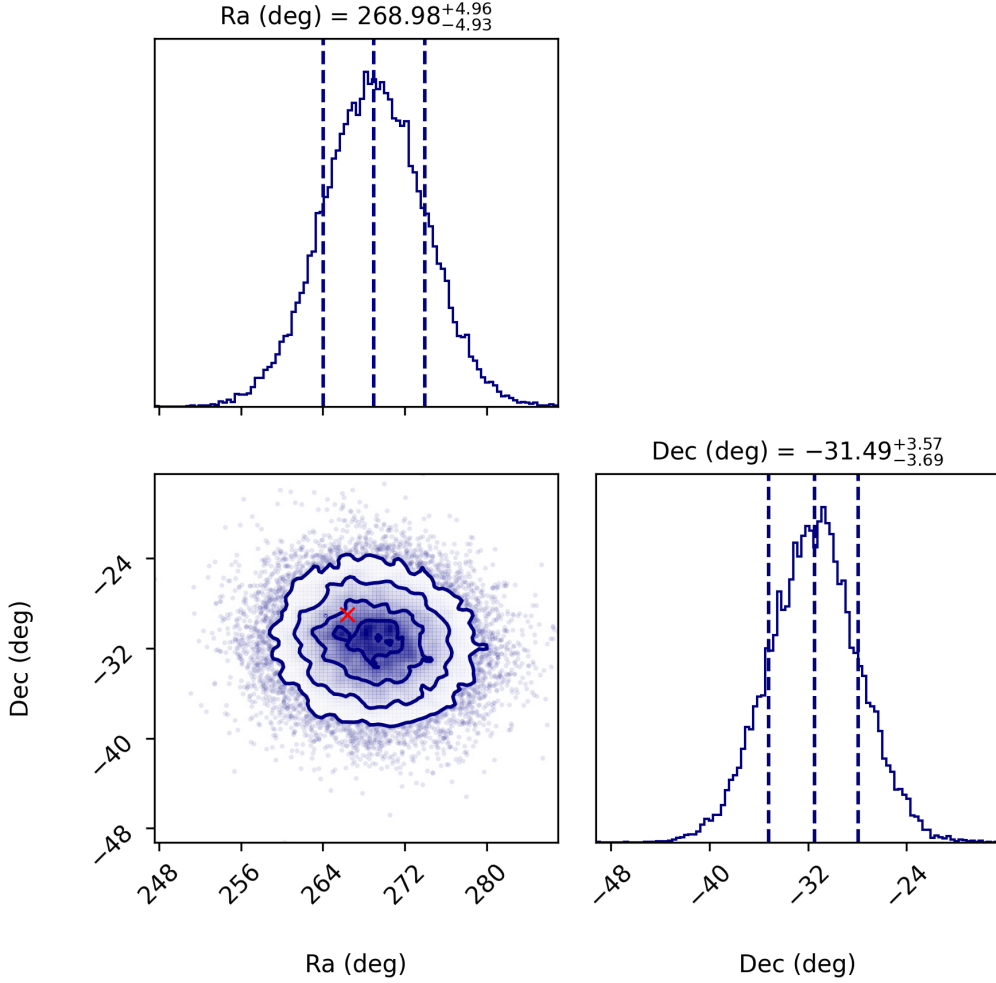


Figure 8: 2D joint distribution of the RA and Dec samples. The red cross indicates the location of the Galactic centre, located at $\alpha \approx 266.42^\circ$, $\delta \approx -29.01$ (M. J. Reid and Brunthaler, 2004).

5.2 Further Tests

To extend the analysis beyond what was presented in Klioner et al. (2021), we computed the power spectral distribution (PSD) of each toroidal and spheroidal VSH coefficient. Additionally, we applied the HMC sampling algorithm to both the full five-parameter Gaia EDR3 dataset (unfiltered) and two filtered versions, using stricter outlier rejection thresholds: a more aggressive clipping value of $\kappa = 2.0$ and a more lenient one of $\kappa = 4.0$.

5.2.1 Power Spectral Distribution (PSD) of VSH Coefficients

To assess the contribution of each harmonic degree, we computed the power spectral distribution (PSD) for both toroidal and spheroidal VSH components, sampled from the same filtered dataset used to determine the results displayed in Table 1, as shown in Figures 9.

The PSD quantifies the power carried by each l -mode of the VSH expansion. As expected, the total power increases with l_{\max} , indicating that higher-order harmonics capture additional structure in the data. In particular, power plateaus after $l = 5$ for both components, suggesting that systematics beyond this scale may contribute less significantly or are absorbed into noise.

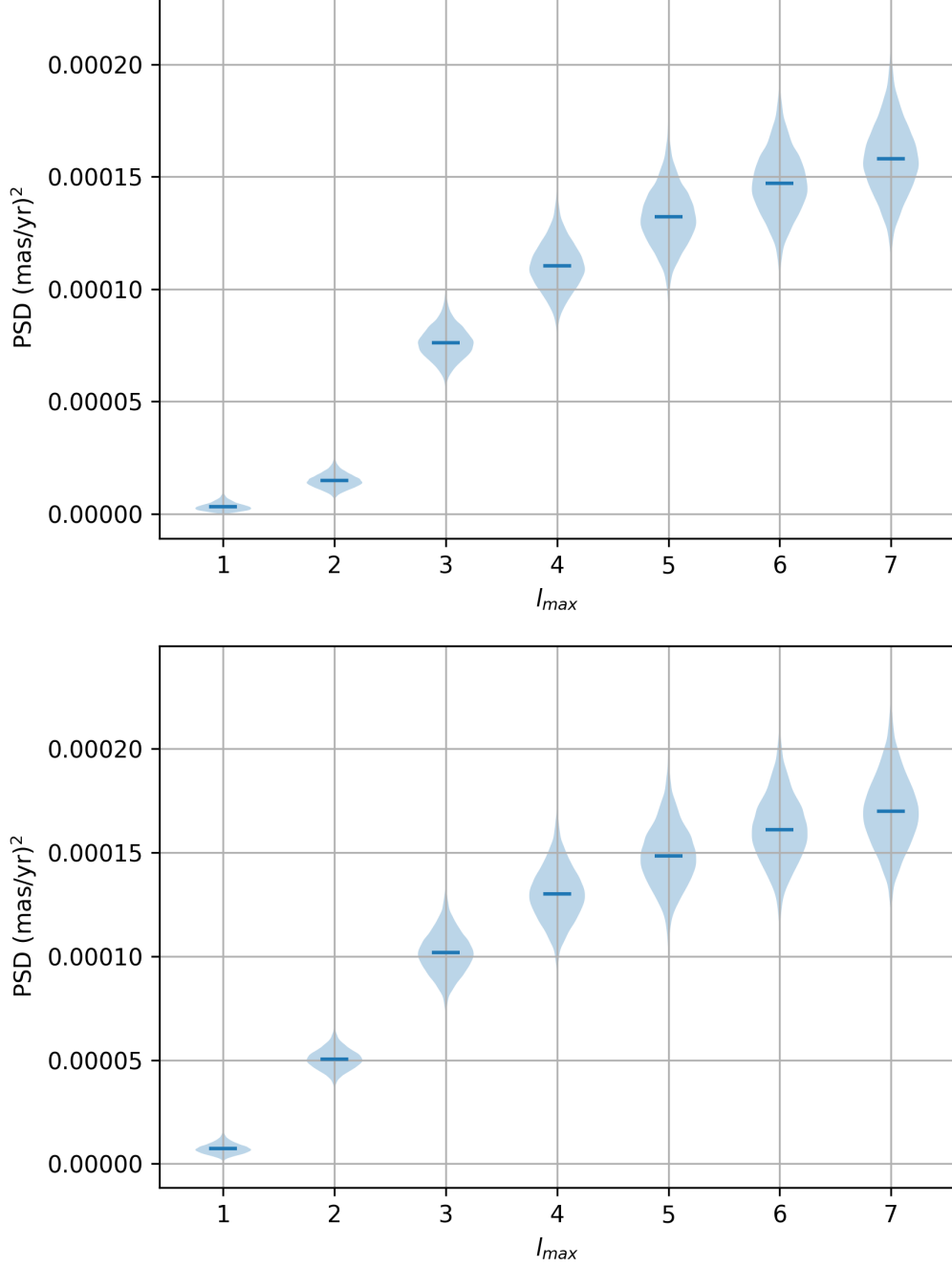


Figure 9: Violin plots showing the power spectral distribution (PSD) of the VSH coefficient samples as a function of harmonic degree l_{\max} . The top panel corresponds to the toroidal components, and the bottom panel to the spheroidal components. Each distribution reflects the spread and median of the posterior power for each l mode.

The similarity in behaviour between the toroidal and the spheroidal components supports the assumption that both capture comparable levels of large-scale systematics. These results reinforce the choice of $l_{\max} = 3$ for modelling the glide signal, providing a trade-off between capturing relevant systematics and maintaining computational efficiency.

5.2.2 Impact of Clipping Thresholds on Acceleration Estimates

Outlier rejection through different clipping thresholds ($\kappa = 2$, Table 2, $\kappa = 4$ Table 3 and undefined Table 4) has only a mild effect on the final estimate acceleration vector. Across all configurations, the magnitude of the acceleration remains consistent within uncertainties (all near $\sim 5 \mu\text{as yr}^{-1}$). The

directional components show small variations, but these are also within 1σ bounds. The trend is feasible and expected:

- Stricter filtering (e.g., $\kappa = 2$) removes more sources, potentially reducing contamination or extreme residuals, resulting in slightly tighter uncertainties.
- Softer thresholds or no filtering allow more data in, but the fit remains stable, indicating that the underlying signal is robust against small-scale systematics or outliers.

This robustness across clipping levels reinforces confidence in the validity of the inferred acceleration and suggests that no strong bias is introduced by the choice of κ , as long as some basic level of quality control is applied.

Table 2: Estimate of the Solar System acceleration vector using HMC sampling on data filtered with clipping threshold $\kappa = 2.0$, 79 550 sources were detected as outliers. All uncertainties are at the 1σ level.

Quantity	Value	Uncertainty
<i>Equatorial components</i>		
g_x [$\mu\text{as yr}^{-1}$]	−0.25	0.39
g_y [$\mu\text{as yr}^{-1}$]	−4.17	0.33
g_z [$\mu\text{as yr}^{-1}$]	−2.65	0.33
α [deg]	266.52	5.31
δ [deg]	−32.40	3.91
<i>Correlations</i>		
ρ_{g_x, g_y}	−0.001	
ρ_{g_x, g_z}	−0.088	
ρ_{g_y, g_z}	−0.020	
$\rho_{\alpha, \delta}$	−0.050	
<i>Galactic components</i>		
g_X [$\mu\text{as yr}^{-1}$]	+4.93	0.33
g_Y [$\mu\text{as yr}^{-1}$]	−0.25	0.34
g_Z [$\mu\text{as yr}^{-1}$]	−0.16	0.39
l [deg]	357.09	3.91
b [deg]	−1.89	4.48
<i>Correlations</i>		
ρ_{g_X, g_Y}	+0.029	
ρ_{g_X, g_Z}	−0.016	
ρ_{g_Y, g_Z}	−0.086	
$\rho_{l, b}$	−0.002	
$ \mathbf{g} $ [$\mu\text{as yr}^{-1}$]	4.94	0.33

All results presented in Tables 2, 3, and 4 were obtained using HMC sampling with 8 chains and 5000 samples per chain. Convergence diagnostics confirmed that all parameters successfully converged, with estimated IAT of 2 in each case. Accordingly, we applied thinning by a factor of 2, resulting in a total of 20,000 effective posterior samples used for inference in each dataset.

Table 3: Estimate of the Solar System acceleration vector using HMC sampling on data filtered with clipping threshold $\kappa = 4.0$, 41 sources were detected as outliers. All uncertainties are reported at the 1σ level.

Quantity	Value	Uncertainty
<i>Equatorial components</i>		
g_x [$\mu\text{as yr}^{-1}$]	-0.27	0.37
g_y [$\mu\text{as yr}^{-1}$]	-4.12	0.32
g_z [$\mu\text{as yr}^{-1}$]	-2.85	0.32
α [deg]	266.27	5.15
δ [deg]	-34.58	3.72
<i>Correlations</i>		
ρ_{g_x, g_y}	+0.003	
ρ_{g_x, g_z}	-0.101	
ρ_{g_y, g_z}	-0.020	
$\rho_{\alpha, \delta}$	-0.052	
<i>Galactic components</i>		
g_X [$\mu\text{as yr}^{-1}$]	+4.99	0.32
g_Y [$\mu\text{as yr}^{-1}$]	-0.43	0.32
g_Z [$\mu\text{as yr}^{-1}$]	-0.25	0.37
l [deg]	355.13	3.70
b [deg]	-2.84	4.26
<i>Correlations</i>		
ρ_{g_X, g_Y}	+0.034	
ρ_{g_X, g_Z}	-0.017	
ρ_{g_Y, g_Z}	-0.076	
$\rho_{l, b}$	-0.001	
$ \mathbf{g} $ [$\mu\text{as yr}^{-1}$]	5.02	0.32

Table 4: Estimate of the Solar System acceleration vector using HMC sampling on the full (unfiltered) five-parameter Gaia EDR3 dataset. All uncertainties are reported at the 1σ level.

Quantity	Value	Uncertainty
<i>Equatorial components</i>		
g_x [$\mu\text{as yr}^{-1}$]	-0.27	0.37
g_y [$\mu\text{as yr}^{-1}$]	-4.09	0.32
g_z [$\mu\text{as yr}^{-1}$]	-2.85	0.32
α [deg]	266.19	5.19
δ [deg]	-34.80	3.74
<i>Correlations</i>		
ρ_{g_x, g_y}	+0.000	
ρ_{g_x, g_z}	-0.095	
ρ_{g_y, g_z}	-0.022	
$\rho_{\alpha, \delta}$	-0.049	
<i>Galactic components</i>		
g_X [$\mu\text{as yr}^{-1}$]	+4.96	0.32
g_Y [$\mu\text{as yr}^{-1}$]	-0.44	0.32
g_Z [$\mu\text{as yr}^{-1}$]	-0.25	0.37
l [deg]	354.90	3.72
b [deg]	-2.90	4.27
<i>Correlations</i>		
ρ_{g_X, g_Y}	+0.036	
ρ_{g_X, g_Z}	-0.015	
ρ_{g_Y, g_Z}	-0.081	
$\rho_{l, b}$	-0.001	
$ \mathbf{g} $ [$\mu\text{as yr}^{-1}$]	4.99	0.32

6 Conclusion

We conclude that our attempt to independently reproduce the results of Klioner et al. (2021) was successful. Using a Bayesian inference framework, we obtained acceleration estimates that closely match the original findings in both magnitude and uncertainty. This demonstrates not only the robustness of the Gaia EDR3 data but also the reliability of alternative inference approaches in recovering the solar system’s acceleration signal (compare Table 1 to Table 2, Section 7 of Klioner et al. (2021)). In addition to reproducing the original results, we conducted further analyses to assess the stability and reliability of the signal. By varying the outlier rejection threshold and computing the power spectral distribution (PSD) of the VSH coefficients, we verified that the inferred acceleration remains consistent across filtering levels and harmonic degrees. These additional tests reinforce the credibility of both our findings and those reported in Klioner et al. (2021), lending further support to the detection of the solar system’s acceleration using Gaia astrometry.

References

- Abuter, R., Amorim, A., Bauböck, M., Berger, J., Bonnet, H., Brandner, W., Clénet, Y., Du Foresto, V. C., De Zeeuw, P., Dexter, J., et al. (2019). A geometric distance measurement to the galactic center black hole with 0.3% uncertainty. *Astronomy & Astrophysics*, 625, L10.
- Bland-Hawthorn, J., & Gerhard, O. (2016). The galaxy in context: Structural, kinematic, and integrated properties. *Annual Review of Astronomy and Astrophysics*, 54(1), 529–596.
- Burbidge, G., & Perry, J. (1976). On the masses of the quasi-stellar objects. *Astrophysical Journal*, vol. 205, Apr. 15, 1976, pt. 2, p. L55-L58. *NSF-supported research*; 205, L55–L58.
- Eilers, A.-C., Hogg, D. W., Rix, H.-W., Frankel, N., Hunt, J. A., Fouvy, J.-B., & Buck, T. (2020). The strength of the dynamical spiral perturbation in the galactic disk. *The Astrophysical Journal*, 900(2), 186.
- ESA, F. (1997). The hipparcos and tycho catalogues. *ESA SP*, 1200.
- Fabrizius, C., Luri, X., Arenou, F., Babusiaux, C., Helmi, A., Muraveva, T., Reylé, C., Spoto, F., Vallenari, A., Antoja, T., et al. (2021). Gaia early data release 3-catalogue validation. *Astronomy & Astrophysics*, 649, A5.
- Fanselow, J., & Sovers, O. (1985). Observation model and parameter partial for the jpl vlbi parameter estimation software” masterfit-v2. 0”. *Jet Propulsion Lab. Report*, 8339.
- Hunt, J. A., Bub, M. W., Bovy, J., Mackereth, J. T., Trick, W. H., & Kawata, D. (2019). Signatures of resonance and phase mixing in the galactic disc. *Monthly Notices of the Royal Astronomical Society*, 490(1), 1026–1043.
- Katz, D., Antoja, T., Romero-Gómez, M., Drimmel, R., Reylé, C., Seabroke, G. M., Soubiran, C., Babusiaux, C., Di Matteo, P., Figueras, F., et al. (2018). Gaia data release 2-mapping the milky way disc kinematics. *Astronomy & Astrophysics*, 616, A11.
- Klioner, S. A., Mignard, F., Lindegren, L., Bastian, U., McMillan, P. J., Hernández, J., Hobbs, D., Ramos-Lerate, M., Biermann, M., Bombrun, A., et al. (2021). Gaia early data release 3-acceleration of the solar system from gaia astrometry. *Astronomy & Astrophysics*, 649, A9. https://www.aanda.org/articles/aa/full_html/2021/05/aa39734-20/aa39734-20.html
- Lindegren, L., Hernández, J., Bombrun, A., Klioner, S., Bastian, U., Ramos-Lerate, M., De Torres, A., Steidelmüller, H., Stephenson, C., Hobbs, D., et al. (2018). Gaia data release 2-the astrometric solution. *Astronomy & Astrophysics*, 616, A2.
- Lindegren, L., Klioner, S., Hernández, J., Bombrun, A., Ramos-Lerate, M., Steidelmüller, H., Bastian, U., Biermann, M., de Torres, A., Gerlach, E., et al. (2021). Gaia early data release 3-the astrometric solution. *Astronomy & Astrophysics*, 649, A2.
- Malkin, Z. (2014). On the implications of the galactic aberration in proper motions for the celestial reference frame. *Monthly Notices of the Royal Astronomical Society*, 445(1), 845–849.
- McMillan, P. J. (2011). Mass models of the milky way. *Monthly Notices of the Royal Astronomical Society*, 414(3), 2446–2457.
- McMillan, P. J. (2016). The mass distribution and gravitational potential of the milky way. *Monthly Notices of the Royal Astronomical Society*, stw2759.
- Mignard, F., & Klioner, S. (2012). Analysis of astrometric catalogues with vector spherical harmonics. *Astronomy & Astrophysics*, 547, A59. <https://www.aanda.org/articles/aa/pdf/2012/11/aa19927-12.pdf>
- Monari, G., Famaey, B., Siebert, A., Grand, R. J., Kawata, D., & Boily, C. (2016). The effects of bar–spiral coupling on stellar kinematics in the galaxy. *Monthly Notices of the Royal Astronomical Society*, 461(4), 3835–3846.
- Pérez-Villegas, A., Portail, M., Wegg, C., & Gerhard, O. (2017). Revisiting the tale of hercules: How stars orbiting the lagrange points visit the sun. *The Astrophysical Journal Letters*, 840(1), L2.
- Perryman, M., & van Leeuwen, F. (1995). Future possibilities for astrometry in space. *Future Possibilities for Astrometry in Space*, 379.
- Pond, J. (1833). A catalogue of 1112 stars, reduced from observations made at the royal observatory at greenwich, eng from the years 1816 to 1833. *Astronomical Observations made at the Royal Observatory at Greenwich*, vol. 18, pp. PI-P19, 18.
- Prusti, T., De Bruijne, J., Brown, A. G., Vallenari, A., Babusiaux, C., Bailer-Jones, C., Bastian, U., Biermann, M., Evans, D. W., Eyer, L., et al. (2016). The gaia mission. *Astronomy & Astrophysics*, 595, A1.
- Reid, M. J., & Brunthaler, A. (2004). The proper motion of sagittarius a*. ii. the mass of sagittarius a. *The Astrophysical Journal*, 616(2), 872.

- Reid, M., & Brunthaler, A. (2020). The proper motion of sagittarius a*. iii. the case for a supermassive black hole. *The Astrophysical Journal*, 892(1), 39.
- Reid, M., Menten, K., Brunthaler, A., Zheng, X., Dame, T., Xu, Y., Wu, Y., Zhang, B., Sanna, A., Sato, M., et al. (2014). Trigonometric parallaxes of high mass star forming regions: The structure and kinematics of the milky way. *The Astrophysical Journal*, 783(2), 130.
- Schönrich, R., Binney, J., & Dehnen, W. (2010). Local kinematics and the local standard of rest. *Monthly Notices of the Royal Astronomical Society*, 403(4), 1829–1833.
- Wegg, C., Gerhard, O., & Portail, M. (2015). The structure of the milky way’s bar outside the bulge. *Monthly Notices of the Royal Astronomical Society*, 450(4), 4050–4069.

A Use of Auto-Generation Tools

A.1 Copilot

GitHub Copilot was used to assist with the writing of function docstrings and some descriptive comments throughout the project repository. Suggestions were accepted passively via autocomplete rather than through explicit prompts or instructions.

A.2 Chat-GPT4

Chat-GPT4 was used for, providing insights and suggestions for improving the structure and functionality of the code. Generating concise and accurate summaries of complex texts to enhance understanding and clarity.

B Trace Plots

Trace plots are visual diagnostics used to assess MCMC convergence. They display the sampled values of each parameter across iterations for each chain. Well-mixed, overlapping traces that resemble “hairy caterpillars” suggest convergence, while trends, drifts, or lack of mixing may indicate problems like non-convergence or poor sampling. We only used trace plots for our main analysis (Table 1) Figure 10, as other check were conducted for other experiments.

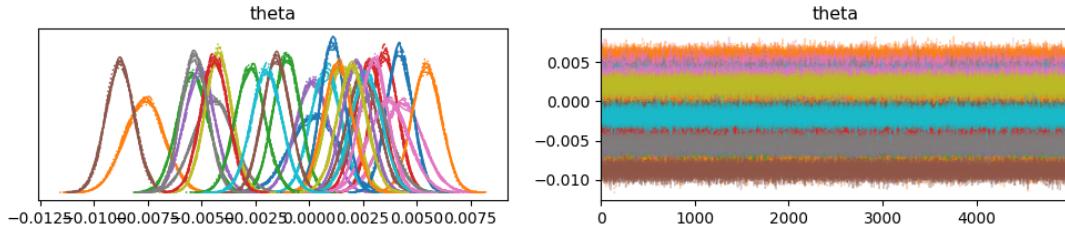


Figure 10: Left: Posterior distributions of the VSH coefficients (parameter θ) obtained from all chains. Right: Corresponding trace plots for each parameter across iterations, illustrating chain mixing and convergence.

As we can see from Figure 10, the chains mix well and explore the posterior distribution efficiently, indicating that the algorithm is working correctly and effectively traversing the likelihood surface. To produce trace plots, we used the Python package [Arviz](#).

C Different Prior

As previously mention, we also tried to run the HMC sampling algorithm with a different prior. The prior in question is a uniform distribution in range $[-1, 1]$, this is also a suitable choice. Our objective was to further test the model robustness. As hoped, the choice of prior did not affect the result and performance, as shown in Table 5, if we compare this with Table 1, Section 5, in main report, we can see that the parameter estimates are almost identical.

Table 5: Estimate of the Solar System acceleration vector using HMC sampling with uniform prior.

Quantity	Value	Uncertainty
<i>Equatorial components</i>		
g_x [$\mu\text{as yr}^{-1}$]	−0.08	0.37
g_y [$\mu\text{as yr}^{-1}$]	−4.30	0.32
g_z [$\mu\text{as yr}^{-1}$]	−2.65	0.32
α [deg]	268.97	4.97
δ [deg]	−31.62	3.66
<i>Correlations</i>		
ρ_{g_x, g_y}	−0.008	
ρ_{g_x, g_z}	−0.095	
ρ_{g_y, g_z}	−0.012	
$\rho_{\alpha, \delta}$	−0.037	
<i>Galactic components</i>		
g_X [$\mu\text{as yr}^{-1}$]	+5.04	0.32
g_Y [$\mu\text{as yr}^{-1}$]	−0.10	0.32
g_Z [$\mu\text{as yr}^{-1}$]	−0.29	0.37
l [deg]	358.82	3.67
b [deg]	−3.27	4.22
<i>Correlations</i>		
ρ_{g_X, g_Y}	+0.039	
ρ_{g_X, g_Z}	−0.022	
ρ_{g_Y, g_Z}	−0.090	
$\rho_{l, b}$	−0.002	
$ \mathbf{g} $ [$\mu\text{as yr}^{-1}$]	5.05	0.32

The close agreement of results obtained with different priors demonstrates that the data are sufficiently informative, and the inference is robust to prior assumptions. This indicates that the final estimates are primarily driven by the data, reducing the potential for prior-induced bias and supporting the reliability of the model.